Journal of Computational Physics 228 (2009) 2847–2858

Contents lists available at ScienceDirect

Journal of Computational Physics

journal homepage: www.elsevier.com/locate/jcp

Spectral difference method for compressible flow on unstructured grids with mixed elements

Chunlei Liang [a,*], Antony Jameson [a], Z.J. Wang [b]

[a] Aeronautics and Astronautics, Stanford University, Durand Building 358, Stanford, CA 94305, USA
[b] Department of Aerospace Engineering, Iowa State University, Ames, IA 50011, USA

ARTICLE INFO

Article history:
Received 22 July 2008
Received in revised form 24 November 2008
Accepted 28 December 2008
Available online 16 January 2009

Keywords:
Spectral difference method
Curved wall boundary
Unstructured grid
Mixed elements

ABSTRACT

This paper presents the development of a 2D solver for inviscid and viscous compressible flows using the spectral difference (SD) method for unstructured grids with mixed elements. A mixed quadrilateral and triangular grid is first refined using one-level *h*-refinement to generate a quadrilateral grid while keeping the curvature of boundary edges. The SD method designed for quadrilateral meshes can subsequently be applied for the refined unstructured grid. Results obtained with the SD method for both inviscid and viscous compressible flows compare well with analytical solutions and other published results.

Published by Elsevier Inc.

1. Introduction

The spectral difference method is a newly developed efficient high-order approach based on the differential form of governing equations. It was originally proposed by Liu et al. [10] and developed for wave equations in their paper on triangular grids. Wang et al. [19] extended it to 2D Euler equations on triangular grids and [7] improved the convergence of the method using implicit LU-SGS and *p*-multigrid schemes. Some additional contributions are made by May and Jameson [11] and Huang et al. [4]. Recently, [17] further developed it for three-dimensional Navier–Stokes equations on hexahedral unstructured meshes. The SD method combines elements from finite-volume and finite-difference techniques. Similar to the discontinuous Galerkin (DG) [1,2] and spectral volume (SV) methods [20,21], the SD scheme achieves high-order accuracy by locally approximating the solutions as a high degree polynomial inside each cell. However, being based on the differential form of the equations, its formulation is simpler than that of the DG and SV methods as no test function or surface integral is involved. Conservation properties are still maintained by a judicious placement of the nodes at quadrature points of the chosen simplex.

Generating unstructured grids using simply quadrilateral elements sometimes is not so straightforward although one may want to keep quadrilateral elements to resolve a boundary layer. One alternative way in unstructured grid generation is to use mixed quadrilateral and triangular elements. To apply the SD method on unstructured mixed elements, one approach is to design two different sets of cardinal basis functions for triangles and quadrangles respectively and another approach is to perform one-level *h*-refinement to convert a mixed-element grid to a quadrilateral organization. In this paper, the later is employed.

For 2D quadrilateral and three-dimensional hexahedral grids based on multi-domain approach, the SD method is identical to the multi-domain spectral method proposed in [6]. One of the key motivations of the present paper is to extend the SD

* Corresponding author. Tel.: +1 650 724 5479.
E-mail address: chliang@stanford.edu (C. Liang).

0021-9991/$ - see front matter Published by Elsevier Inc.
doi:10.1016/j.jcp.2008.12.038

method to fully-unstructured grids. While doing this, a flexible and robust algorithm is also developed for high-order representation of curved boundaries similar to [21].

The paper is organized as follows: Section 2 describes the numerical approach and solution methods. In order to validate the spatial accuracy of the code, Section 3 presents two cases with analytical solutions. Section 4 reports the simulation results obtained for inviscid subsonic flow past a NACA 0012 airfoil. Section 5 demonstrates the computational results for unsteady viscous flow past an elliptic cylinder. Finally, some conclusions are drawn in Section 6.

2. Numerical formulation

2.1. h-refinement

The initial unstructured grids are formed by either triangular or quadrilateral elements. One can refine the elements using their centroids and edge middle points. As shown in Fig. 1, one can split a triangular element to three quadrilateral elements. It is also shown in Fig. 2, a quadrilateral element can be partitioned into four quadrilateral elements. When an element lies on a curved boundary, a cubic spline fitting subroutine is implemented to shift the edge middle point on the curved boundary. As shown in Fig. 3, a spline curve is determined by curve fitting over four points, $p0, p1, p2$ and $p3$. The middle point pc sits in the middle of points $p1$ and $p2$. The other edge middle points are simply the averaged values of corner points of the element $(p1 - p2 - pb - pa)$.

2.2. SD spatial discretization

The SD method on 2D quadrilateral elements is simpler than that on 2D triangular elements because it involves only one-dimensional polynomials to construct flux values from solution points and to calculate derivatives on solution points from fluxes, etc. In other words, the method allows one to use polynomial interpolation based on tensor product forms rather than the multivariate interpolation used with triangular elements. It is therefore also simple in order to extend it for unstructured hexahedral grids [17]. A baseline 2D code using only quadrilateral elements has been developed and validated by Liang et al. [8]. Premasuthan et al. [14] extended this code to have implicit LU-SGS time marching scheme and a p-multigrid method for accelerating solution speed. Liang et al. [9] further developed it as a three-dimensional SD code and simulated a turbulent channel flow.

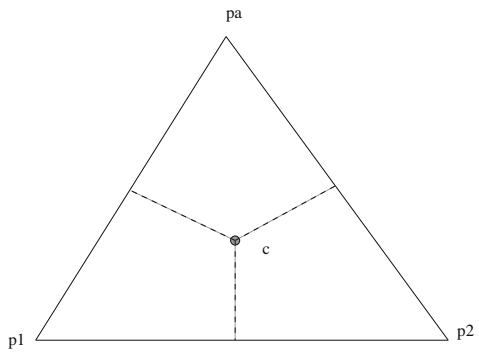

Fig. 1. Refinement of a triangular cell with straight edges.

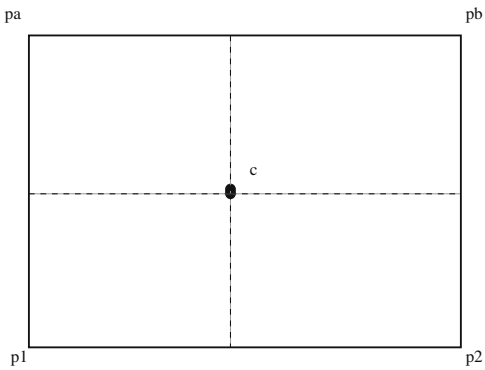

Fig. 2. Refinement of a quadrilateral cell with straight edges.

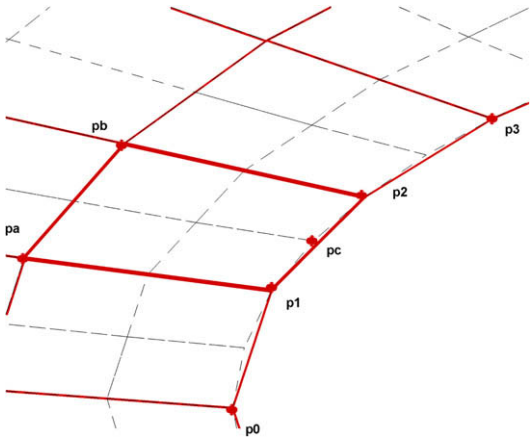

Fig. 3. Refinement of a near-wall quadrilateral cell.

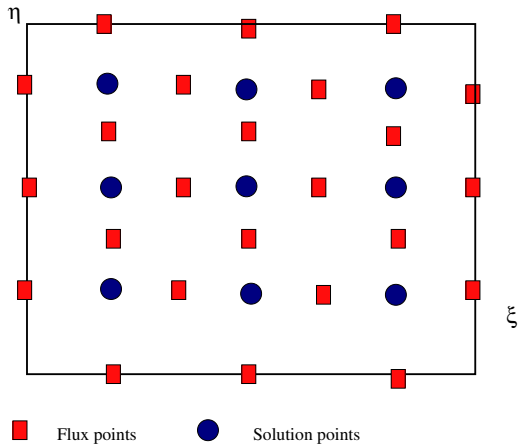

Fig. 4. Distribution of flux and solution points for the third order SD scheme.

Consider the unsteady compressible 2D Navier–Stokes equations in conservative form

$$\frac{\partial Q}{\partial t}+\frac{\partial F}{\partial x}+\frac{\partial G}{\partial y}=0, \tag{1}$$

where Q is the vector of conserved variables; F and G are the total fluxes including both inviscid and viscous flux vectors. To achieve an efficient implementation, all quadrilateral elements in the physical domain (x,y) determined by the one-level h-refinement are transformed into a standard square element $(0\leqslant\xi\leqslant 1, 0\leqslant\eta\leqslant 1)$ as shown in Fig. 4. The transformation can be written as:

$$\begin{pmatrix} x \\ y \end{pmatrix}=\sum_{i=1}^{K} M_i(\xi,\eta)\begin{pmatrix} x_i \\ y_i \end{pmatrix}, \tag{2}$$

where K is the number of points used to define the physical element, (x_i, y_i) are the cartesian coordinates of those points, and $M_i(\xi,\eta)$ are the shape functions. For elements with straight edges, K is equal to 4. For elements lying on curved boundaries, 8 points (four mid-edge and four corner points) can define a quadratic representation and 12 points can define a third-order cubic representation. The metrics and the Jacobian of the transformation can be computed for each element. The governing equations in the physical domain are then transferred into the computational domain, and the transformed equations take the following form:

$$\frac{\partial \tilde{Q}}{\partial t}+\frac{\partial \tilde{F}}{\partial \xi}+\frac{\partial \tilde{G}}{\partial \eta}=0, \tag{3}$$

where $\tilde{Q} = |J| \cdot Q$, $J = \begin{pmatrix} x_\xi & x_\eta \\ y_\xi & y_\eta \end{pmatrix}$ and

$$\begin{pmatrix} \tilde{F} \\ \tilde{G} \end{pmatrix} = |J| J^{-1} \begin{pmatrix} F \\ G \end{pmatrix}. \tag{4}$$

In the standard element, two sets of points are defined, namely the solution points and the flux points, as illustrated in Fig. 4.

In order to construct a degree $(N-1)$ polynomial in each coordinate direction, solution at N points are required. The solution points in one-dimensional are chosen to be the Chebyshev–Gauss points defined by:

$$X_s = \frac{1}{2}\left[1 - \cos\left(\frac{2s-1}{2N} \cdot \pi\right)\right], \quad s = 1, 2, \ldots, N. \tag{5}$$

The flux points are selected to be the Chebyshev–Gauss–Lobatto points given by

$$X_{s+1/2} = \frac{1}{2}\left[1 - \cos\left(\frac{s}{N} \cdot \pi\right)\right], \quad s = 0, 1, \ldots, N. \tag{6}$$

van den Abeele et al. [18] pointed out the weak instability of the choice of Chebyshev–Gauss–Lobatto points for flows with periodic boundaries. Nevertheless, the instability is not witnessed in our simulations in this paper. Alternatively, the flux points can be selected as the Legendre–Gauss-quadrature points plus the two end points, 0 and 1, as suggested by Huynh [5] in order eliminate the weak instability. It will be stated out explicitly whenever the Legendre–Gauss-quadrature points are used in this paper.

Using the solutions at N solution points, a degree $(N-1)$ polynomial can be built using the following Lagrange basis defined as:

$$h_i(X) = \prod_{s=0, s \neq i}^{N} \left(\frac{X - X_s}{X_i - X_s}\right). \tag{7}$$

Similarly, using the fluxes at $(N+1)$ flux points, a degree N polynomial can be built for the flux using a similar Lagrange basis defined as:

$$l_{i+1/2}(X) = \prod_{s=0, s \neq i}^{N} \left(\frac{X - X_{s+1/2}}{X_{i+1/2} - X_{s+1/2}}\right). \tag{8}$$

The reconstructed solution for the conserved variables in the standard element is just the tensor products of the two one-dimensional polynomials,

$$Q(\xi, \eta) = \sum_{j=1}^{N} \sum_{i=1}^{N} \frac{\tilde{Q}_{i,j}}{|J_{i,j}|} h_i(\xi) \cdot h_j(\eta). \tag{9}$$

Similarly, the reconstructed flux polynomials take the following form:

$$\begin{aligned} \tilde{F}(\xi, \eta) &= \sum_{j=1}^{N} \sum_{i=0}^{N} \tilde{F}_{i+1/2,j} l_{i+1/2}(\xi) \cdot h_j(\eta), \\ \widetilde{G}(\xi, \eta) &= \sum_{j=0}^{N} \sum_{i=1}^{N} \widetilde{G}_{i,j+1/2} h_i(\xi) \cdot l_{j+1/2}(\eta). \end{aligned} \tag{10}$$

The reconstructed fluxes are only element-wise continuous, but discontinuous across cell interfaces. For the inviscid flux, a Riemann solver is employed to compute a common flux at interfaces to ensure conservation and stability. In our case, we have used the Rusanov solver [15] to compute the interface fluxes. The Rusanov scheme takes the following form

$$\widehat{F} = 1/2[(F_L + F_R) \cdot \mathbf{n} - \lambda(Q_R - Q_L)], \tag{11}$$

where $\lambda = |V_n| + c$ is an upper bound for the absolute values of the characteristic speeds. V_n is the fluid velocity normal to edge interface and c is the sound speed.

In summary, the algorithm to compute the inviscid flux derivatives consists of the following steps:

(1) Given the conservative variables at the solution points, the conservative variables are computed at the flux points.
(2) The inviscid fluxes at the interior flux points are computed using the solutions computed at Step (1).
(3) The inviscid fluxes at the element interfaces are computed using the Rusanov solver. Given the normal direction of the interface n, and the averaged normal velocity component V_n and the sound speed c, the inviscid flux on the interface can be determined.
(4) The derivatives of the fluxes are computed at the solution points using the derivatives of Lagrange operators l

$$\begin{aligned}\left(\frac{\partial \tilde{F}}{\partial \xi}\right)_{i,j} &= \sum_{r=0}^{N} \tilde{F}_{r+1/2,j} \cdot l'_{r+1/2}(\xi_i),\\ \left(\frac{\partial \tilde{G}}{\partial \eta}\right)_{i,j} &= \sum_{r=0}^{N} \tilde{G}_{i,r+1/2} \cdot l'_{r+1/2}(\eta_j)\end{aligned} \tag{12}$$

2D Navier–Stokes equations can be written in conservation form as the following:

$$\frac{\partial Q}{\partial t} + \nabla F_e(Q) - \nabla F_v(Q, \nabla Q) = 0, \tag{13}$$

where the conservative variables Q and Cartesian components $f_e(Q)$ and $g_e(Q)$ of the inviscid flux vector $F_e(Q)$ are given by

$$Q = \begin{Bmatrix} \rho \\ \rho u \\ \rho v \\ E \end{Bmatrix}, \quad f_e(Q) = \begin{Bmatrix} \rho u \\ \rho u^2 + p \\ \rho u v \\ u(E+p) \end{Bmatrix}, \quad g_e(Q) = \begin{Bmatrix} \rho v \\ \rho u v \\ \rho v^2 + p \\ v(E+p) \end{Bmatrix}. \tag{14}$$

Here ρ is the density, u and v are the velocity components in x and y directions, p stands for pressure and E is the total energy. The pressure is related to the total energy by

$$E = \frac{p}{\gamma - 1} + \frac{1}{2}\rho(u^2 + v^2) \tag{15}$$

with a constant ratio of specific heat γ. For all test cases in the present study, γ is going to be 1.4 for air.

The Cartesian components $f_v(Q, \nabla Q)$ and $g_v(Q, \nabla Q)$ of viscous flux vector $F_v(Q, \nabla Q)$ are given by

$$\begin{aligned} f_v(Q, \nabla Q) &= \mu \begin{Bmatrix} 0 \\ 2u_x + \lambda(u_x + v_y) \\ v_x + u_y \\ u[2u_x + \lambda(u_x + v_y)] + v(v_x + u_y) + \frac{C_p}{P_r} T_x \end{Bmatrix},\\ g_v(Q, \nabla Q) &= \mu \begin{Bmatrix} 0 \\ v_x + u_y \\ 2v_y + \lambda(u_x + v_y) \\ v[2v_y + \lambda(u_x + v_y)] + u(v_x + u_y) + \frac{C_p}{P_r} T_y \end{Bmatrix}, \end{aligned} \tag{16}$$

where μ is the dynamic viscosity, C_p is the specific heat and P_r stands for Prandtl number. T is temperature which can be derived from the perfect gas assumption. λ is set to $-2/3$ according to the Stokes hypothesis.

The solution procedures to get viscous fluxes can be described as the following steps.

- Reconstruct $Q_{k,c}$ at the flux points from the conservative variables at the solution points using Eq. (9).
- Average the field of $Q_{k,c}$ on the element interfaces as $\overline{Q_f} = \frac{1}{2}(Q^L_{k,c} + Q^R_{k,c})$. Meanwhile, boundary conditions shall be applied for u, v and T.
- Evaluate ∇Q from $\overline{Q_f}$ using Eq. (12) where $\nabla Q = \begin{Bmatrix} Q_x \\ Q_y \end{Bmatrix}$ and $Q_x = \frac{\partial Q}{\partial \xi}\xi_x + \frac{\partial Q}{\partial \eta}\eta_x$, etc.
- Reconstructing ∇Q from Eq. (9), average them on the element interfaces as $\overline{\nabla Q_f} = \frac{1}{2}(\nabla Q^L_{k,i} + \nabla Q^R_{k,i})$
- use $\overline{Q_f}$ and $\overline{\nabla Q_f}$ in order to compute viscous flux vectors described in Eq. (16) at the element interfaces.

The subscript k refers to the flux points and subscript c stands for cell number.

2.3. Time marching scheme

Flows with either steady or unsteady solutions are considered in this paper. In order to solve the flow to a steady state from a nearly arbitrary initial guess, a relaxation scheme is needed. Therefore, the time derivative term is kept for all cases. All computations in this paper are advanced in time using a fourth-order strong-stability-preserving five-stage Runge–Kutta scheme [16].

3. Accuracy validation

In the following, an inviscid flow case and a viscous flow case with analytical solutions are selected in order to demonstrate the order of accuracy of the implemented SD method. In order to obtain independent results for different time step sizes, we reduce the time step size by a certain factor until L_2 error reaches a constant which is independent the Δt.

3.1. Validation using supersonic vortex flow

The supersonic vortex flow problem is one of the few non-trivial problems of the compressible 2D Euler equations for which a smooth analytical solution is known. The inviscid, isentropic, supersonic flow of a compressible fluid between concentric circular arcs presents a flow where the velocity varies inversely with radius. The expression for density as a function of radius r is given by:

$$\rho(r) = \rho_i \left\{ 1 + \frac{\gamma - 1}{2} Ma_i^2 \left[1 - \left(\frac{r_i}{r} \right)^2 \right] \right\}^{\frac{1}{\gamma - 1}}, \tag{17}$$

where Ma_i and r_i are the Mach number and the radius at the inner arc. In the present calculation, the Mach number, density and pressure at the inner radius r_i are specified to be $2.25, 1$ and $1/\gamma$, respectively. The inner and outer radii are 1 and 1.384. The outer arc and bottom boundaries are fixed with analytical solutions. The zero-gradient extrapolation boundary is employed for the exit. In the following, the numerical solution to this problem are computed for second-, third- and fourth-order SD method on successively refined grids. All the computations are initialized using constant density and pressure. The $L2$ error of the density is evaluated.

The three meshes used in the computation are shown in Fig. 5. The initial triangular meshes are having 6, 24 and 96 elements, respectively. One-level h-refinement transforms these meshes into quadrilateral ones as shown in Fig. 6 with 18, 72 and 288 elements and the resolution of the curved boundaries is improved. A Mach contour distribution is obtained in Fig. 7 obtained by fourth-order SD method. It is computed on grid c shown in Fig. 5 after one-level h-refinement.

The details of the order calculation and verification are shown in Table 1. The table clearly indicates that the SD method applied to the steady compressible Euler equations exhibits a full order of convergence on smooth solutions. It provides the details of the spatial accuracy of the SD method for fourth-order SD method. One can also see the $L1$ and $L2$ errors of the SD method against the number of DOFs demonstrate that the numerical spatial order is close to four.

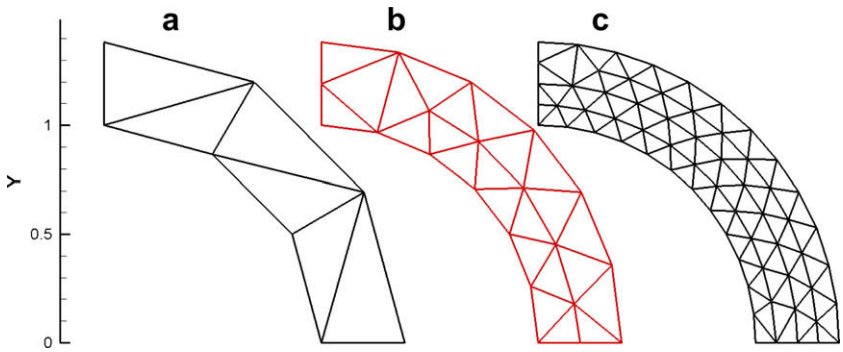

Fig. 5. Initial triangular grids for supersonic vertex flow.

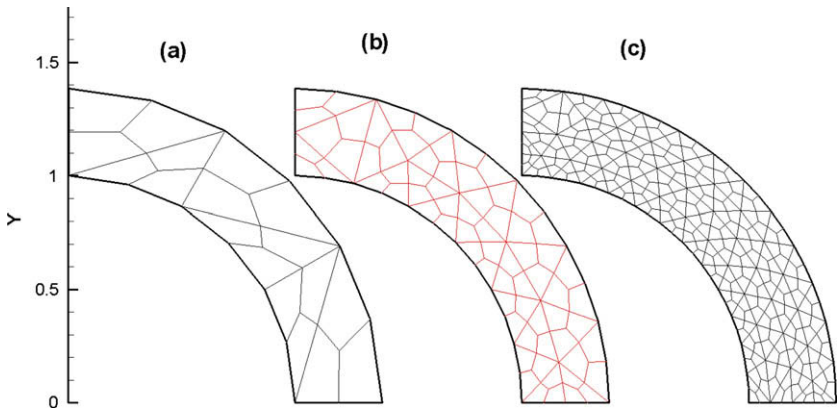

Fig. 6. Quadrilateral computational grids after h-refinement for supersonic vertex flow.

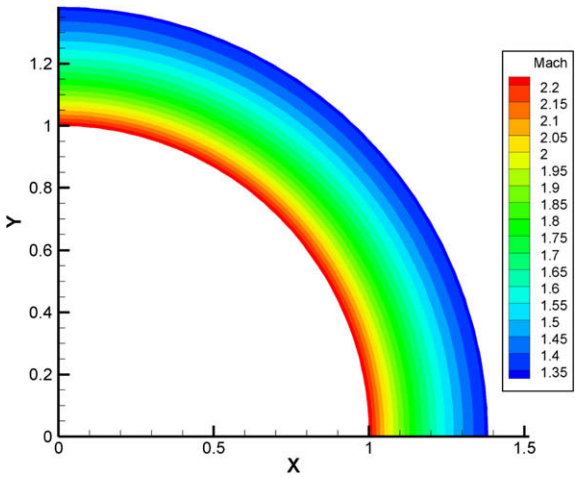

Fig. 7. Mach contour solution obtained using fourth-order accurate SD method.

Table 1
L^1 and L^2 errors and orders of accuracy of inviscid supersonic vertex flow.

No. of elements	No. of DOFs	L1-error	Order	L2-error	Order
Fourth-order SD					
6	288	2.04E–4	–	3.02E–4	–
24	1152	1.29E–5	3.98	1.93E–5	3.97
96	4608	8.62E–7	3.90	1.14E–6	4.08

3.2. Validation using viscous Couette flow

The numerical order of accuracy is validated using compressible Couette flow with analytical solution. The computational domain is a rectangular box ($0 \leqslant x \leqslant 2$ and $0 \leqslant y \leqslant 1$). The coarsest grid has only two quadrilateral elements. The other grids for this test problem are obtained by successive h-refinement of the coarser grid. A periodic boundary condition is used in the stream-wise direction. A moving wall no-slip boundary with constant temperature and a specified external pressure is used for the top surface ($y = H = 1$). A stationary no-slip wall with constant temperature is used for the bottom surface $y = 0$. The exact solutions of the this problem are

$$u = \frac{U}{H}y, \quad v = 0,$$
$$e = e_b + \frac{y}{H}(e_t - e_b) + \frac{PrU^2}{2\gamma}\frac{y}{H}\left(1 - \frac{y}{H}\right); \quad p = \text{const},$$

where Pr is the Prandtl number and $e = C_v T$ is the internal energy. The density ρ is related to pressure p through $\rho = \frac{p}{(\gamma-1)e}$. The subscripts t and b refer to top and bottom surfaces, respectively.

We obtained desired numerical order up to fourth-order accuracy using $L2$ error as shown in Table 2. It demonstrates that the stability and accuracy of SD method on quadrilateral elements in dealing with viscous fluxes.

4. Inviscid flow past NACA 0012

By parameterizing β as $\beta = x^2$, NACA 0012 thickness distribution can be exactly represented by an eighth-order parametric Bezier curve, $y = \pm\frac{t}{0.2}(0.29690\beta - 0.12600\beta^2 - 0.35160\beta^4 + 0.28430\beta^6 - 0.10150\beta^8)$, where t is the maximum thickness. The initial mixed-element mesh is shown in Fig. 8 and the far-field distance is 20 chords. The initial grid is only having 1881 elements. To perform one-level h-refinement and custom high-order curved boundary method for SD method, the Bezier curve was subdivided to match the domain of each edge on the surface of an existing mesh. After one-level h-refinement, a quadrilateral mesh with 5792 elements is obtained. A sectional part of this grid is visualized in Fig. 9. The inviscid case was computed at a Mach number of 0.63 and an angle of attack of 2 degrees by Flores et al. [3]. It is revisited here by a third-order scheme SD method with total DOFs of 52,128. The computation conducted with a third-order curved wall

Table 2
L^2 errors and orders of accuracy of viscous Couette flow.

No. of elements	No. of DOFs	L2-error	Order
Second-order SD			
2	8	1.4180E–02	–
8	32	3.3520E–03	2.081
32	128	9.1210E–04	1.878
128	512	2.4350E–04	1.905
Third-order SD			
2	18	1.4783E–03	–
8	72	1.5199E–04	3.282
32	288	1.6525E–05	3.201
128	1152	1.7991E–06	3.199
Fourth-order SD			
2	32	1.9784E–04	–
8	128	1.1827E–05	4.064
32	512	7.9780E–07	3.890
128	2048	4.7330E–08	4.075

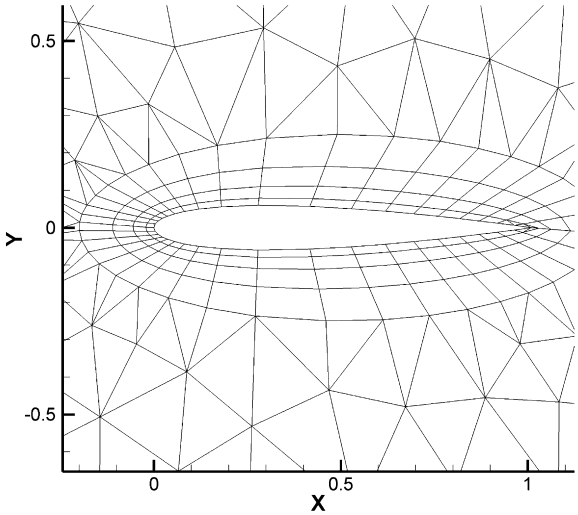

Fig. 8. Initial mixed-element mesh for NACA 0012.

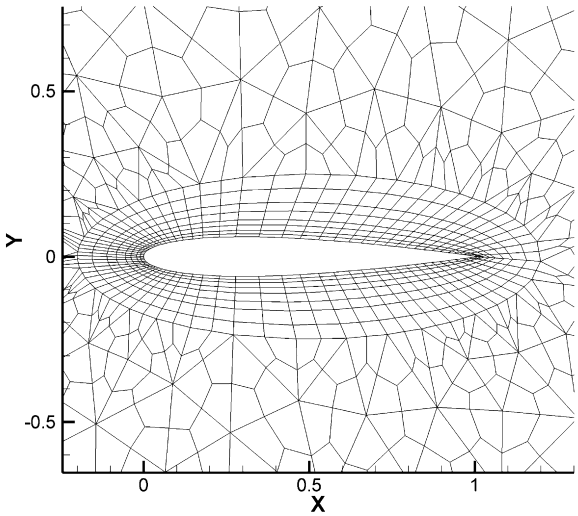

Fig. 9. Quadrilateral mesh after *h*-refinement for NACA 0012.

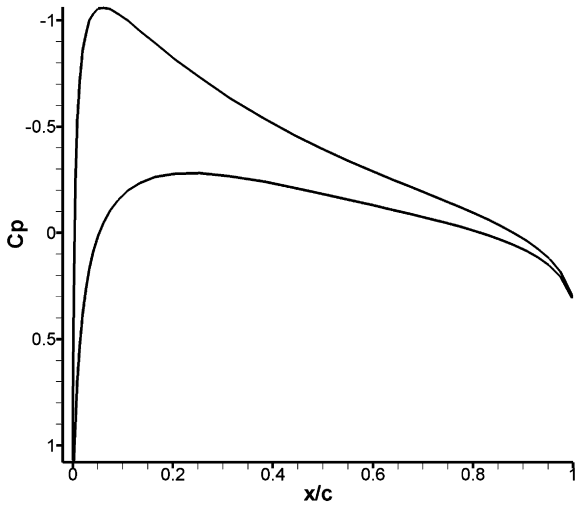

Fig. 10. Pressure coefficient for NACA 0012.

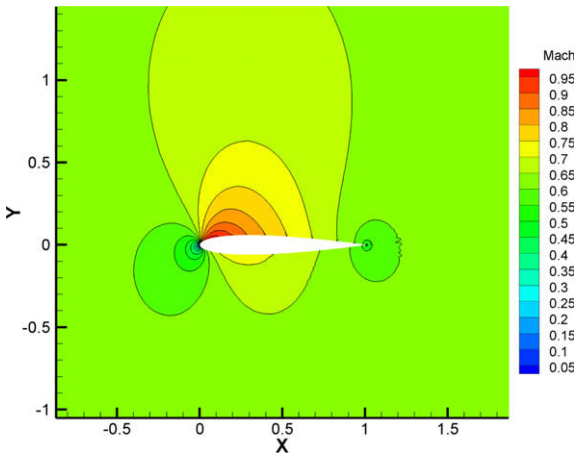

Fig. 11. Mach contour for NACA 0012.

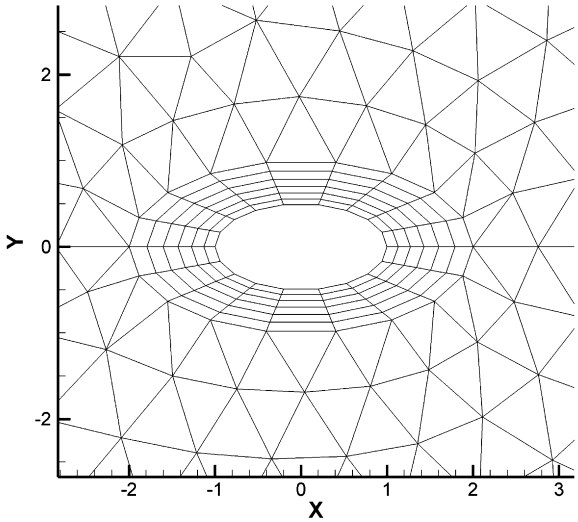

Fig. 12. Initial mixed-element mesh for elliptic cylinder.

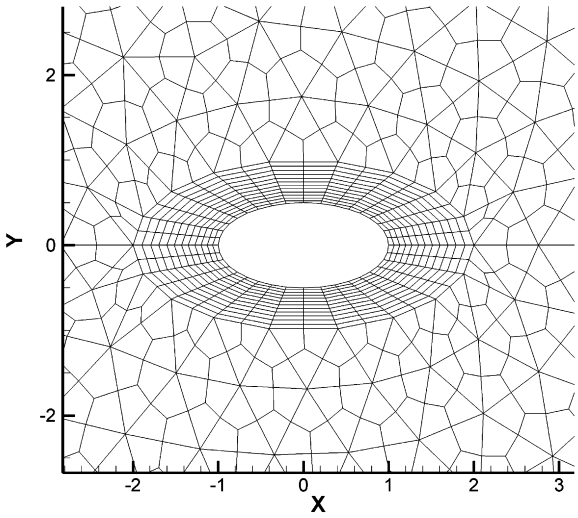

Fig. 13. Quadrilateral mesh after *h*-refinement for elliptic cylinder.

boundary representation. At these conditions, the computed flow is completely subsonic and thus the surface pressure coefficient has a smooth distribution for upper and lower surfaces, respectively (see Fig. 10) and a Mach contour distribution is obtained in Fig. 11 with maximum Mach number less than 1. The predicted lift coefficient is 0.3291 and it is close to 0.3321 obtained in [3] and 0.3253 using a fourth-order scheme on 10,694 CVs in [13].

In the following, the above illustrated ideas are applied to compute unsteady viscous flows.

5. Unsteady viscous flow

In order to compute viscous terms, the quadrilateral elements can avoid placements of flux points on the corner points of the elements. One can thus directly average the fluxes on the connecting edges between elements to deal with discontinuous fields there to obtain $\overline{Q}$ and $\overline{\nabla Q}$ for computing $\nabla F_v(\overline{Q}, \overline{\nabla Q})$. In the following, a testing case examined by Mittal and Balachandar [12] for elliptic cylinder is chosen.

5.1. Flow past an elliptic cylinder

Laminar unsteady incompressible flow past an elliptic cylinder has been studied by Mittal and Balachandar [12] (case 5) at Reynolds number 525 based on projected lateral width L_y^*. The ratio of lateral width and streamwise length L_x is 0.5. It is studied here by a fourth-order SD method and a third-order curved wall boundary representation in our computation. The initial grid with mixed elements is shown in Fig. 12. The total DOFs are 45,600 on a grid of 2850 quadrilateral elements as shown in Fig. 13 after *h*-refinement of an unstructured grid with only 914 mixed elements. The freestream velocity is 0.1 m/s and Mach number is 0.1 giving a nearly incompressible flow condition. The projected lateral width is 1 in our computational mesh. Uniform time-stepping is used and the time step size gives $\Delta t \times U_\infty / L_y^* = 8 \times 10^{-5}$. Legendre–Gauss-quadrature points are used for this test case. This test case with Chebyshev–Gauss–Lobatto points using the same time step size diverges in the end.

As shown in Table 3, the mean drag coefficient predicted by SD method is 0.787 which agrees well with the value of 0.78 predicted by Mittal and Balachandar [12] on a mesh with total number grid of 12,960 using a Fourier–Chebyshev collocation scheme for spatial discretization. The Strouhal number $St^* = fL_y^*/U_\infty = 0.21$ predicted by SD method is identical to the one predicted by Mittal and Balachandar [12]. One instantaneous vorticity shedding contour is shown in Fig. 14. Surface pressure coefficient is plotted against x/L_y^* in Fig. 15. At this time instant, after separation point, C_p is higher for the upper surface than lower surface because the lower side is associated with lower pressure.

Table 3
Statistics of flow past elliptic cylinders predicted by fourth-order SD against [12] using Fourier–Chebyshev collocation scheme.

Investigator	No. of elements	C_d	St^*	C_l'
Mittal 1996	12,960	0.78	0.21	–
Present	2850	0.785	0.21	0.43

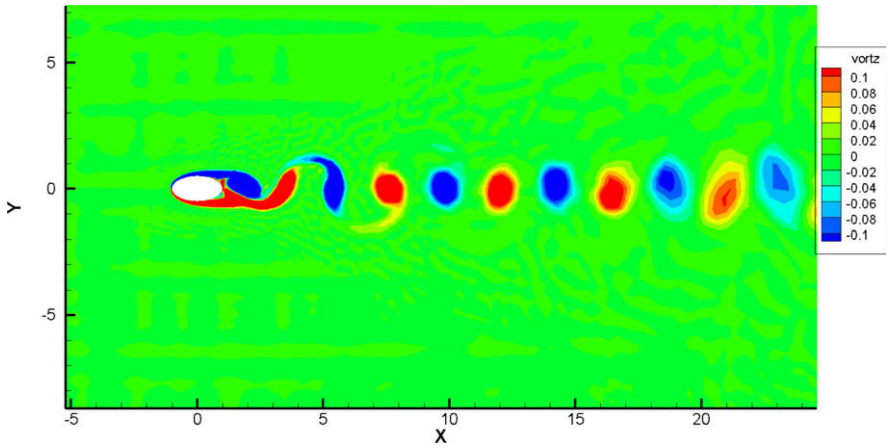

Fig. 14. Vorticity shedding behind the elliptic cylinder.

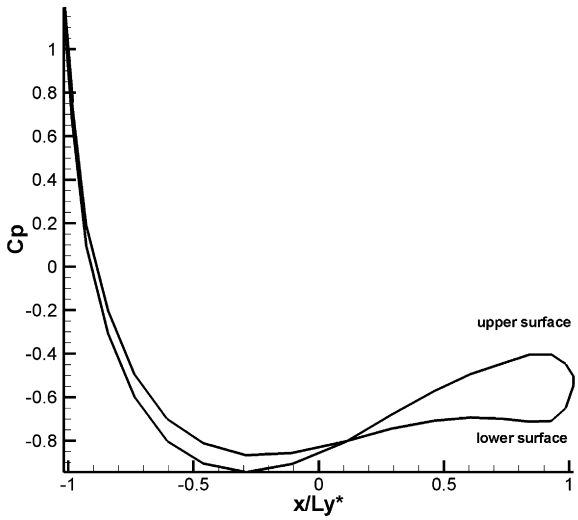

Fig. 15. Surface pressure coefficient for the elliptic cylinder.

6. Conclusion

A 2D unstructured spectral difference solver is developed for both inviscid and viscous flows. The SD method designed for quadrilateral grids is successfully extended to unstructured meshes with mixed elements after one-level *h*-refinement while maintaining the spatially high-order numerical properties. High-order curved boundary representations are implemented for performing both *h*-refinement and high-order SD scheme discretization of the cells connecting to the wall boundaries. This algorithm can be extended to three-dimensional mixed tetrahedral and hexahedral elements.

Acknowledgment

The first two authors would like to thank the grant support from NSF with award No. 0708071 monitored by Leland Jameson.

References

[1] F. Bassi, S. Rebay, High-order accurate discontinuous finite element solution of the 2D Euler equations, Journal of Computational Physics 138 (1997) 251–285.
[2] B. Cockburn, C.-W. Shu, The Runge–Kutta discontinuous Galerkin method for conservation laws V: Multidimensional systems, Journal of Computational Physics 141 (1998) 199–224.
[3] J. Flores, J. Barton, T. Holst, T. Pulliam, Comparison of the full-potential and euler formulations for computing transonic airfoil flows, in: E.A.H. Araki (Ed.), Ninth International Conference on Numerical Methods in Fluid Dynamics, vol. 218, 1985, pp. 213–218.

[4] P.G. Huang, Z.J. Wang, Y. Liu, An implicit space-time spectral difference method for discontinuity capturing using adaptive polynomials, AIAA paper 2005-5255, 2005.
[5] H. Huynh, A flux reconstruction approach to high-order schemes including discontinuous Galerkin methods, AIAA PaperAIAA-2007-4079, 2007.
[6] D.A. Kopriva, A conservative staggered-grid Chebyshev multidomain method for compressible flows. II A semi-structured method, Journal of Computational Physics 128 (1996) 475–488.
[7] C. Liang, R. Kannan, Z.J. Wang, A p-multigrid spectral difference method with explicit and implicit smoothers on unstructured triangular grids, Computers and Fluids 38 (2009) 254–265.
[8] C. Liang, S. Premasuthan, A. Jameson, High-order accurate simulation of low-mach laminar flow past two side-by-side cylinders using spectral difference method, Computers and Structures (2009), in press.
[9] C. Liang, S. Premasuthan, A. Jameson, Z.J. Wang, Large eddy simulation of compressible turbulent channel flow with spectral difference method, In: 47th AIAA Aerospace Sciences Meeting including The New Horizons Forum and Aerospace Exposition, AIAA Paper 2009-402, Orlando, Florida, Jan. 5-8, 2009.
[10] Y. Liu, M. Vinokur, Z.J. Wang, Spectral difference method for unstructured grids I: Basic formulation, Journal of Computational Physics 216 (2006) 780–801.
[11] G. May, A. Jameson, A spectral difference method for the Euler and Navier–Stokes equations, AIAA paper 2006-2304, 2006.
[12] R. Mittal, S. Balachandar, Direct numerical simulation of flow past elliptic cylinders, Journal of Computational Physics 124 (1996) 351–367.
[13] A. Nejat, C. Ollivier-Gooch, A high-order accurate unstructured finite volume Newton–Krylov algorithm for inviscid compressible flows, Journal of Computational Physics 227 (2008) 2582–2609.
[14] S. Premasuthan, C. Liang, A. Jameson, Z.J. Wang, p-Multigrid spectral difference method for viscous compressible flow using 2D quadrilateral meshes, In: 47th AIAA Aerospace Sciences Meeting including The New Horizons Forum and Aerospace Exposition, AIAA Paper 2009-950, Orlando, Florida, Jan. 5-8, 2009.
[15] V.V. Rusanov, Calculation of interaction of non-steady shock waves with obstacles, Journal of Computational Math Physics USSR 1 (1961) 261–279.
[16] R.J. Spiteri, S.J. Ruuth, A new class of optimal high-order strong-stability-preserving time discretization methods, SIAM Journal of Numerical Analysis 40 (2002) 469–491.
[17] Y. Sun, Z.J. Wang, Y. Liu, High-order multidomain spectral difference method for the Navier–Stokes equations on unstructured hexahedral grids, Communication in Computational Physics 2 (2007) 310–333.
[18] K. van den Abeele, C. Lacor, Z.J. Wang, On the stability and accuracy of the spectral difference method, Journal of Scientific Computing (2008), doi:10.1007/s10915-008-9201-0.
[19] Z. Wang, Y. Liu, G. May, A. Jameson, Spectral difference method for unstructured grids II: Extension to the Euler equations, Journal of Scientific Computing 32 (2007) 45–71.
[20] Z.J. Wang, Spectral (finite) volume method for conservation laws on unstructured grids basic formulation basic formulation, Journal of Computational Physics 178 (2002) 210–251.
[21] Z.J. Wang, Y. Liu, Extension of the spectral volume method to high-order boundary representation, Journal of Computational Physics 211 (2006) 154–178.